Journal of Science and Technology in Civil Engineering, HUCE, 2024, 18 (3): 48–59

CRACK PATTERNS IN MASONRY STRUCTURES USING PHASE FIELD METHOD

Nguyen Thi Hai Nhu[a,*], Tran Anh Binh[a]

[a]*Faculty of Information Technology, Hanoi University of Civil Engineering, 55 Giai Phong road, Hai Ba Trung district, Hanoi, Vietnam*

Article history:
Received 11/3/2024, Revised 25/4/2024, Accepted 22/5/2024

Abstract

This work aims to study the crack pattern in masonry-like structures by a simplified description of the medium using a variational damage model. In literature, when modeling fractures in masonry structures, capturing both fracture types, cracks in units, and cracks at the interface simultaneously, usually requires a complicated scheme. The phase-field method has been widely used recently because of its robustness in capturing various fracture types. In this work, we consider the mortar and the interface (between the mortar and units) as a thick interface layer with pseudo-material properties. We conduct numerical tests on a bending beam and a tensile wall using strategies of material properties with a phase field model. As it is not distinguished the crack in the mortar and the brick-mortar interface, it is shown in this work that both types of fracture, in the thick interface layer and the unit, can be captured just using the phase field method and the simplified micro model.

Keywords: masonry structures; cracks; propagation; damage; phase field.

https://doi.org/10.31814/stce.huce2024-18(3)-04

1. Introduction

Masonry is one of the oldest construction structures. While advances have been made in building materials to enhance their properties, the fundamental components of masonry remain unchanged, primarily consisting of two main ingredients: units and mortar. For units, the elastic and fracture properties can vary since they can be made of clay, concrete, stone, or other innovative materials. Damage in this structure may result from external loads, especially lateral loads such as earthquakes (see [1]), material shrinkage, and boundary inhomogeneities. Although masonry structures are not commonly employed as load-bearing components in modern construction, they remain valuable in many urban areas where high-rise buildings are less prevalent, and structures made from local materials are favored. Moreover, the preservation of many historic structures necessitates an understanding and prediction of the behavior of masonry works.

Recent progress in modeling damage in masonry structures can be classified into three groups as shown in Fig. 1(a)-(c): (1) macro modeling, where masonry units and mortar phases are considered homogeneous using homogenization techniques [2–5]; (2) micro-modeling [6, 7] with distinct elements and constitutive laws for the masonry units, mortar joints, and interfaces between units and mortar; (3) simplified micro-models [8, 9] where structures are composed of blocks and interfaces between blocks only. While the micro model can lead to difficulties in tracking geometry, the macro model homogenizes the medium and cannot capture the zig-zag cracks in this type of structure. The simplified micro model in the literature usually examines the interaction between individual units and require tracking geometry during computation. To reduce this burden for simulation, this work suggests a simplified model where the interface and the mortar are treated as a thick interface layer as in Fig. 1(c).

*Corresponding author. *E-mail address:* nhunth@huce.edu.vn (Nhu, N. T. H.)

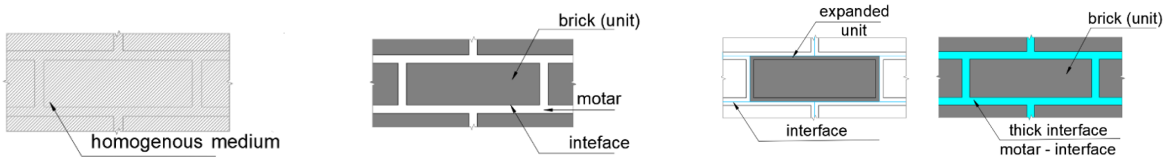

(a) Macro model (b) Micro model (c) simplified micro models

Figure 1. Modeling of masonry medium: (a) homogenized medium with 1 phase description; (b) micro model with 3 phase description and (c) simplified description with 2 phases: thin interface [8, 9] and thick interface (mortar-interface) in this work

Modeling the propagation of cracks in heterogeneous mediums is not a straightforward task due to inherent nonlinearity. In many structures, material uncertainties can lead to varying results, and accurately predicting post-peak behavior is rare. For heterogeneous materials, damage models offer advantages over discrete models, as seen in [10]. Utilizing continuum theory, damage models employ one or several damage variables in constitutive formulas to describe material degradation. As no node or element is embedded, the medium remains continuous, and cracks cannot be sharp and separate. However, cracks can simultaneously initiate at multiple positions in the object without any predefined path.

Recently, phase field models [11–13] have been widely used in crack studies for several reasons: they are thermodynamically consistent, damage laws can be ignored, and there are no broadening discontinuities as other damage models. Nevertheless, when applied to modeling a structure, significant computational efforts may be required. Additionally, although there are formulas to select an internal length associated with all damage models for satisfactory stress-strain relations, the results may lead to an unsuitable mesh size. Wu et al. [14] treated the internal length as a geometric parameter only, requiring a cohesive law, and the medium is not purely continuous. This study does not aim to solve the mentioned problem but examines masonry-like structures as a continuous medium for crack tracking using the phase field method.

Since the simplified descriptions in the literature, where blocks are usually expanded to the center of mortar, lead to difficulties tracking interfaces, this study suggests using the mortar phase as a thick interface with modified material parameters. The ability of the phase field model to capture a variety of crack patterns when material properties change will be discussed. The next section briefly reviews a phase field model, followed by Section 3 detailing numerical implementation. Section 4 shows numerical examples and discusses the results. The last section includes conclusions and some remarks.

2. Phase field model for crack tracking

2.1. Energy formula

In this section, a variational approach to the fracture will be introduced. Considering a cracked body in a domain $\Omega \subset \mathbb{R}^3$ containing sharp cracks denoted as Γ, the internal energy formula by Frankford and Marigo [15] can be rewritten as:

$$E_{int} = \int_{\Omega} \Psi(\boldsymbol{\varepsilon}, \Gamma) d\Omega + g_c \int_{\Gamma} d\Gamma \tag{1}$$

where $\Psi(\boldsymbol{\varepsilon}, \Gamma)$ is the elastic strain density function, g_c is the critical energy release rate of materials. In the right part of (1), the first term is called elastic energy and the second term is considered as the dissipated energy. As the crack is unknown, computing the latter is a cumbersome task. To overcome

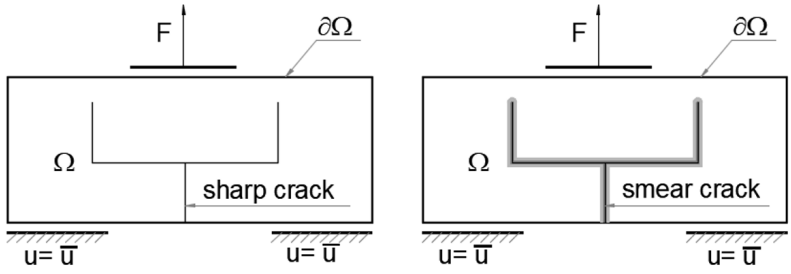

Figure 2. A domain with a sharp crack (a) and a smear crack(b)

this difficulty, Bourdin et al. in [16] has proposed a smeared representation of a sharp crack. The total internal energy is now rewritten as

$$E_{int} = \int_{\Omega} \Psi(\boldsymbol{\varepsilon}, s) d\Omega + g_c \int_{\Omega} \gamma(s, \nabla s) d\Omega \tag{2}$$

where γ is a crack density function which can be chosen among several possible forms. In this regularized framework, the crack is described by a smooth field $s(\mathbf{x})$ ranging from 0 to 1, which represents the intact state to the total damaged state respectively. A popular form for the crack density function is:

$$\gamma(s, \nabla s) = \frac{1}{c}\left[\frac{\omega(s)}{\ell} + \ell \nabla s \cdot \nabla s\right] \tag{3}$$

where ℓ is called the regularized length. This parameter controls the transition zone shapes and is interpreted as a material parameter [11, 12] or a geometry parameter in some other phase field models. A family of crack density functions can be used in (3) written as $\omega(s) = \xi s + (1 - \xi)s^2$. For the simplicity, $\xi = 0$ and $c = 2$ herein, which yields to:

$$\delta\gamma(s, \nabla s) = \frac{s\delta s}{\ell} + \ell \nabla s \cdot \nabla \delta s \tag{4}$$

The total energy of the system is written as:

$$E_{total} = E_{int} + E_{ext} \tag{5}$$

where

$$E_{ext} = -\int_{\Omega} \mathbf{b} \cdot \mathbf{u} d\Omega - \int_{\partial\Omega} \mathbf{f}^* \cdot \mathbf{u} d\partial\Omega \tag{6}$$

In the absence of the body force, the weak form of (5) is derived as:

$$\delta E_{total} = \int_{\Omega} \left(\frac{\partial \Psi}{\partial \boldsymbol{\varepsilon}} : \boldsymbol{\varepsilon} + \frac{\partial \Psi}{\partial s}\delta s\right) d\Omega + g_c \int_{\Omega} \delta\gamma(s, \nabla s)\delta d\Omega - \int_{\partial\Omega} \mathbf{f}^* \delta \mathbf{u} d\partial\Omega \tag{7}$$

To eliminate the appearance of an unphysical crack in the compression zone, the elastic energy density function is separated into a positive part Ψ^+ and a negative part Ψ^- with a degradation function enters the formula and affects the positive part only:

$$\Psi(\boldsymbol{\varepsilon}, s) = g(s)\Psi^+(\boldsymbol{\varepsilon}) + \Psi^-(\boldsymbol{\varepsilon}) \tag{8}$$

It is necessary that the degradation function should monolithically increase from 0 to 1 as the damage field vary from the damage state to the intact state while the function should reach the stationary point when the totally fracture occurs. This results in $g(1) = 0; g(0) = 1; g'(1) = 0$. A popular choice of degradation function is adopted in this work:

$$g(s) = (1 - s)^2 \tag{9}$$

In implementation, to avoid singularity a small k parameter will enter (9) and the $g(s) = (1-s)^2+k$. Though, k is not mandatory in all the cases, in this study, it equals 1×10^{-6}. For an isotropic medium, Miehe proposed to compute the positive and the negative part of elastic energy density using spectral decomposition:

$$\Psi^{\pm}(\boldsymbol{\varepsilon}) = \lambda(\langle Tr(\boldsymbol{\varepsilon})\rangle_{\pm})^2/2 + \mu Tr\{(\boldsymbol{\varepsilon}^{\pm})^2\} \tag{10}$$

where

$$\boldsymbol{\varepsilon}_{\pm} = \sum_{i=1}^{n} \langle Tr(\boldsymbol{\varepsilon})\rangle_{\pm} \mathbf{v}_i \otimes \mathbf{v}_i \tag{11}$$

in which, $\mathbf{v}_i$ are the eigenvectors of the strain tensor $\boldsymbol{\varepsilon}$.

For implementation, the damage field and the displacement field will be solved separately in a staggered scheme by using the Legendre transformation:

$$D_{\delta s} E_{total} = 0, \text{ and } D_{\delta u} E_{total} = 0 \tag{12}$$

where

$$D_{\delta \mathbf{v}} f(\mathbf{u}) = \left\{ \frac{f}{d\alpha} \left(f\left(\mathbf{u} + \alpha \delta \mathbf{v}\right)\right)\right\}_{\alpha=0} \tag{13}$$

2.2. The mechanical problem

$$\int_{\Omega} \frac{\partial \Psi}{\partial \boldsymbol{\varepsilon}}(\boldsymbol{\varepsilon}, s) : \boldsymbol{\varepsilon}(\delta \mathbf{u}) d\Omega - \int_{\partial \Omega_F} \mathbf{f}^* \cdot \delta \mathbf{u} d\Gamma = 0 \tag{14}$$

where

$$\frac{\partial \Psi}{\partial \boldsymbol{\varepsilon}}(\boldsymbol{\varepsilon}, s) = \boldsymbol{\sigma} \tag{15}$$

The strong-form associated with Eq. (11) is written as:

$$\begin{cases} \nabla \cdot \boldsymbol{\sigma} = 0 & \text{in } \Omega \\ \boldsymbol{\sigma}.\mathbf{n} = \mathbf{f}^* & \text{on } \partial\Omega_f \\ \mathbf{u} = \mathbf{u}^* & \text{on } \partial\Omega_u \end{cases} \tag{16}$$

where $\mathbf{n}$ is the outward normal to the boundary.

2.3. The phase field problem

Minimizing (5) according to s leads to:

$$\int_{\Omega} \frac{\partial \Psi}{\partial s} \delta s d\Omega + g_c \int_{\Omega} \delta \gamma(s, \nabla s) d\Omega = 0 \tag{17}$$

or

$$\int_{\Omega} \left\{ \frac{\partial \Psi}{\partial s} \delta s + g_c \left(\frac{s \delta s}{\ell} + \ell \nabla s \cdot \nabla(\delta s) \right) \right\} d\Omega = 0 \tag{18}$$

with regarding (10) and (11), leading to

$$\int_{\Omega}\left\{\left(-2(1-s)\left[\Psi^{+}\right]+\frac{g_c}{\ell}s\right)\delta s+\ell g_c\nabla s\cdot\nabla(\delta s)\right\}d\Omega=0 \tag{19}$$

or

$$\int_{\Omega}\left(2\left[\Psi^{+}\right]+\frac{g_c}{\ell}\right)s\delta s+g_c\ell\nabla s\cdot\nabla(\delta s)d\Omega=\int_{\Omega}2\left[\Psi^{+}\right]\delta s d\Omega \tag{20}$$

Using the divergence theorem

$$\int_{\Omega}g_c\ell\nabla s\cdot\nabla(\delta s)d\Omega=\int_{\partial\Omega}g_c\ell\delta s\nabla s\cdot\mathbf{n}d\Gamma-\int_{\Omega}g_c\ell\Delta s\ \delta s d\Omega \tag{21}$$

(18) becomes

$$\int_{\Omega}\left(2\left[\Psi^{+}\right]+\frac{g_c}{\ell}\right)s\delta s-\lg_c\Delta s\delta s d\Omega=\int_{\Omega}2\left[\Psi^{+}\right]\delta s d\Omega \tag{22}$$

which is the weak form of the following strong form:

$$\begin{cases}\left(2\left[\Psi^{+}\right]+\dfrac{g_c}{\ell}\right)s-\ell g_c\Delta s=2\left[\Psi^{+}\right]\\ \nabla s\cdot\mathbf{n}=0 \quad \text{on } \partial\Omega,\\ s=1 \quad\quad\ \text{on } \Gamma\end{cases} \tag{23}$$

where Δs denotes the Laplacian operator. Enforcing the irreversibility condition using a history function $\mathcal{H}$ has been introduced by Miehe [12] to substitutes to handle loading and unloading and defined as:

$$\mathcal{H}(\mathbf{x},t)=\max_{\tau\in[0,t]}\left\{\Psi^{+}(\mathbf{x},t)\right\} \tag{24}$$

which leads to:

$$\left(2\mathcal{H}+\frac{g_c}{\ell}\right)s-\ell g_c\Delta s=2\mathcal{H},\quad \nabla s\cdot\mathbf{n}=0 \text{ on } \partial\Omega_G,\quad s=1 \text{ on } \Gamma \tag{25}$$

3. Numerical implementation

We denote as the relative error, calculated by

$$R(a_1,a)=\frac{\sqrt{(a_1-a)\times(a_1-a)}}{\sqrt{a\times a}} \tag{26}$$

The Quasi-Newton method will be utilized for the staggered scheme of the coupled problem. The discretized form of displacement field and damage field is written as: $u(\mathbf{x})=\mathbf{N}_u\mathbf{u}$; $\delta u(\mathbf{x})=\mathbf{B}_u\mathbf{u}$ and $s(\mathbf{x})=\mathbf{N}_s\mathbf{s}$; $\delta s(\mathbf{x})=\mathbf{B}_s\mathbf{s}$, where $\mathbf{N}$ and $\mathbf{B}$ is the matrix of shape functions and its derivatives.

4. Numerical tests

In this section, numerical tests will be presented using the simplified model where fracture parameters of the mortar-interface are pseudo. This thick interface has the thickness of the mortar as in Fig. 1(c)). It should be noted that, according to this approach, the interface combines with the mortar to form a new phase. Consequently, the properties of this phase no longer correspond to those of mortar in experiments. The units in masonry structures can be isotropic or anisotropic depending on factors such as shape (with or without holes) or material composition (concrete block, clay brick, etc.). Herein, it is assumed that the unit phase is isotropic. For the case of anisotropic material, other phase field models can be employed to investigate. Plane stress is assumed in the following tests.

With the first load step

- Compute the displacement for intact problem.
- Compute s with u, compute H
- $R = 1;\ u_1 = u;\ s_1 = s;\ iter = 1$
- For i = 2: n step

  $iter = iter+1;$

  + While R > 10^{-5} && iter <=10

    Compute K_u (using d_0)

    Compute F_u

    Compute the displacement field u

    Compute $R = max\,(R(u1,u);\ R(s1,s))$

    Solving damage field: $[\mathbf{K}_s][\boldsymbol{s}] = [\mathbf{F}_s]$,

    $$+\ [\mathbf{K}_s] = \int_\Omega \{(2\mathrm{H} + \frac{g_c}{\ell})[\mathbf{N}_s]^T[\mathbf{N}_s] + g_c\ell[\mathbf{B}_s^T][\mathbf{B}_s]\}\, d\Omega,$$

    $$+\ [\mathbf{F}_s] = 2\int_\Omega [\mathbf{N}_s^T]\mathrm{H}\, d\Omega$$

    $u_1 = u;\ s_1 = s;$

  + End While
- End for

Figure 3. Solving the phase field coupling with mechanics problem using quasi-Newton method

4.1. Bending beam tests

We first study crack patterns of a masonry beam whose structures are similar as the three-point bending test in [14, 17]. The elastic properties of units (bricks) are picked up from [14], while those of the mortar-interface are assumed and to be interpreted as pseudo. The beam is composed of 230 mm × 76 mm × 110 mm bricks. The thickness of the mortar-interface layer is 10 mm. As we consider if the crack pattern changes when the correlation of materials properties varies, the result will not be compared with that of experiments in [17]. The size total geometry of the test is depicted in Fig. 4(a)). Discretization of the beam employs 85,707 triangle elements of the size h = 2 mm ($\ll 0.5l$) in the middle zone where cracks are predicted to appear and of the size 5 mm for other regions. Three cases of materials (B1, B2, B3) are examined (see Table 1). The load is applied by controlling the displacement field at the midpoint on the upper edge of the beam. The internal length equals the thickness of the mortar in all the bending tests.

Table 1. Properties of materials in 3-point bending tests

Test	E_b (Mpa)	E_m/E_b	$v_b = v_m$	g_{cb} (N/mm)	g_{cm}/g_{cb}	Internal length l (mm)
B1	3360	1	0.15	0.06	0.1	10
B2	3360	1	0.15	0.06	0.5	10
B3	3360	0.5	0.15	0.06	0.5	10

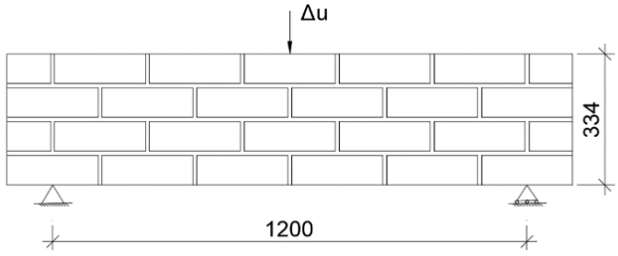

(a) Geometry of there bending tests B1, B2, B3

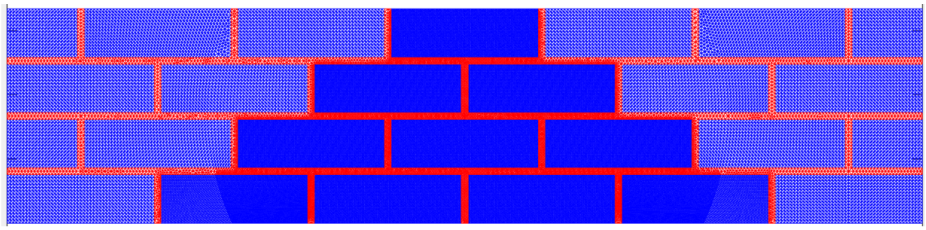

(b) The mesh

Figure 4. Geometry of the test: (a) the structure and the geometry of the beam, the size is in mm and (b) the discretization using finer mesh is applied in the middle zone of the beam where cracks is predicted to appear

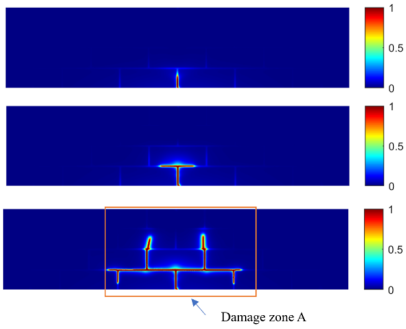

(a) Damage field s

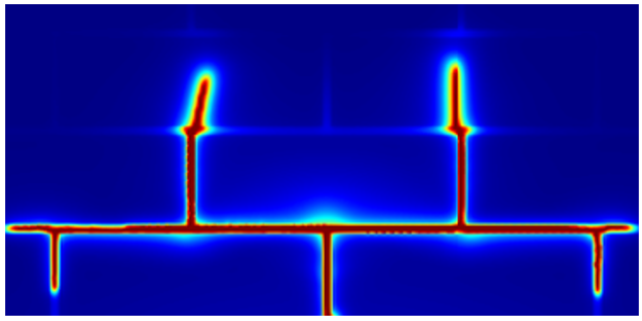

(b) Zoom-in of damage zone A in (a)

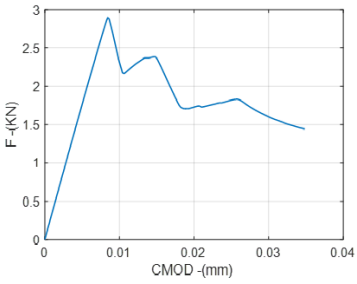

(c) F-CMOD

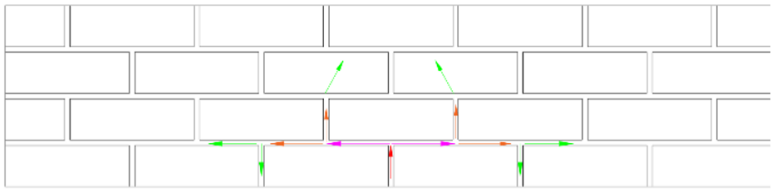

(d) Propagation of cracks

Figure 5. B1 test: (a) from top to bottom: evolution of damage field s, (s = 1 indicates totally damaged); (b) a closed look of damage field (crack pattern) at the end of the simulation; (c) the red arrows at the middle bottom show the initial cracks and, (d) the corresponding F-CMOD curve

In test B1 and B2, 250 load steps have been applied. The load increment Δu is 2×10^{-4} mm for the first 100 steps and 1×10^{-4} mm for the 150 following steps. As the analysis is quasi-static, the load step relates to the convergence of the nonlinear problem only. The fracture toughness of the mortar-interface is 10 times smaller than that of the units ($g_{cm}/g_{cb} = 0.1$) in test B1 while it is a half of the units in B2 test ($g_{cm}/g_{cb} = 0.5$). Fig. 5(a) shows the crack field s of the beam from the onset to the end of the simulation (top to bottom) for test B1. When the fracture toughness of the mortar-interface is extremely weaker (B1), the crack initiates at the middle bottom and then branches along this phase, see Fig. 5(b) for a closer look. The direction of cracks is shown in Fig. 5(d) where cracks penetrate units in the third layer from the bottom. The behavior of F-CMOD curve in Fig. 5(c) reflects a complicated post-peak behavior of the test. Meanwhile, in B2, where the mortar is harder in comparison with B1, after appearing in the mortar-interface phase at the middle bottom, the crack penetrates the unit phase and finally forming a straight crack at the end of simulation as can be seen in Fig. 6(a). It can be observed that when crack evolution straightly to the top, the F-CMOD curve show a smooth degradation.

For test B3, the load increment Δu is 5×10^{-4} mm for the first 50 steps and 2×10^{-4} mm for 250 the following steps. In this test, both the fracture and elastic properties of the mortar-interface are half of those of the units. As shown in the top image of Fig. 6(a), cracks initiate in the same positions as in B1 and B2. However, after branching, a new crack starts in the brick phases and two other cracks start in the mortar-interface separately in the second bottom layer of the beam. It is observed that multiple cracks can be captured, they propagate and connect each other to produce a complex crack in the middle zone of the beam. The load-crack mouth opening displacement (F-CMOD) relation is plotted in Fig. 6(c) shows a double-pick curve. In smeared modes, the CMOD cannot be measured directly but through the displacement of the two lowest points on the left and the right of the beam. Note that, B3 shares the same fracture toughness of material with B2 but using low-strength units.

The results of these tests show that: both elastic properties and fracture toughness significantly affect the propagation of cracks in masonry. The correlation of the stiffness between materials can create a diversity of crack mechanisms

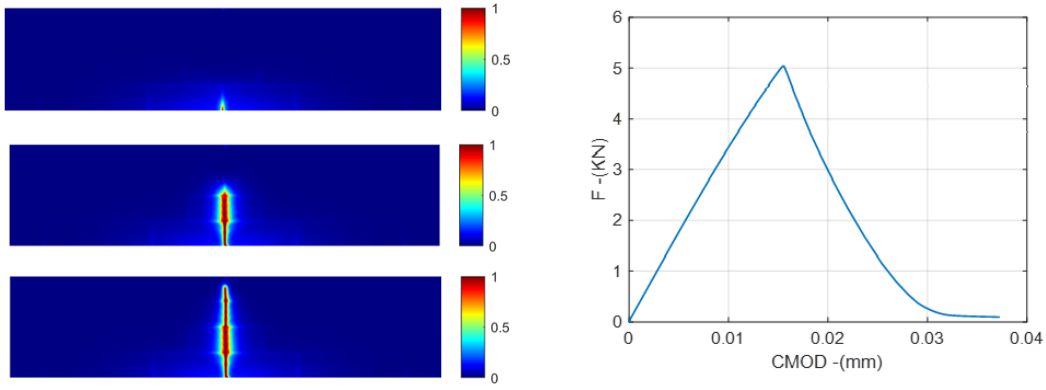

(a) Damage field s (b) F-CMOD

Figure 6. B2 test: (a) from top to bottom: damage field s from the initiation to the end of simulation, and (b) corresponding F-CMOD curve

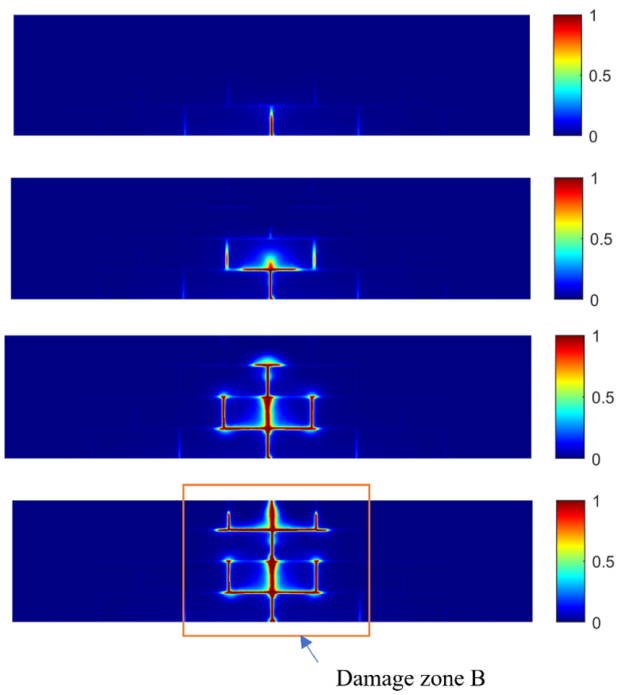

(a) Damage field s

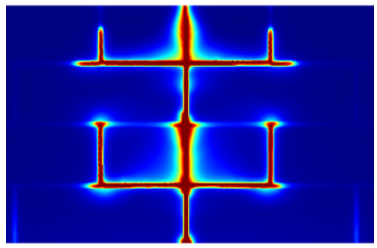

(b) Zoom-in of Damage zone B in (a)

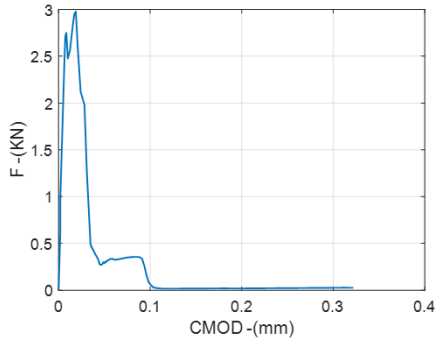

(c) F-CMOD

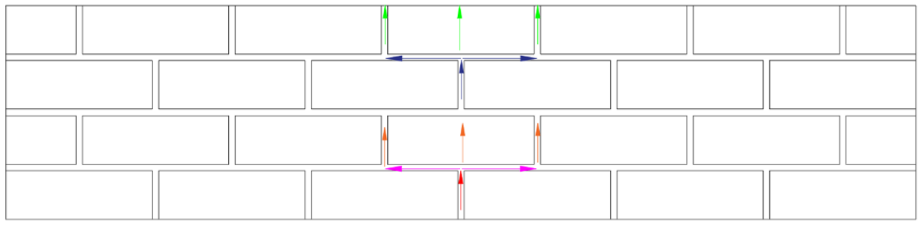

(d) Propagation of cracks

Figure 7. B1 test: (a) from top to bottom: evolution of damage field s, (s = 1 indicates totally damaged); (b) a closed look of damage field (crack pattern) at the end of the simulation; (c) the F-CMOD relation is a double peak curve; (d) the red arrows at the middle bottom show the initial cracks

4.2. Tensile tests

Considering a wall of size 505 mm × 495 mm as depicted in Fig. 8, which comprises four layers of units measuring 240 mm × 115 mm × 110 mm each. We adopt the same configuration as described in literature [18]. Tensile tests are conducted by increasing the displacement equally and simultaneously on both the left and right sides of the wall. The discretization utilizes 56081 triangular elements with a size of 3 mm, as shown in Figs. 9(a), (b). Since the stress-strain curves is out of scope of this study, on the other hand, there is not enough material properties for the model, we

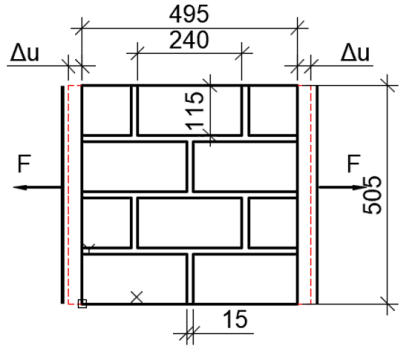

Figure 8. Geometry and configuration of tensile tests (the dimension is in millimet)

use some properties of bricks E_b, g_{cb} and ν_b in [14] and varies other values.

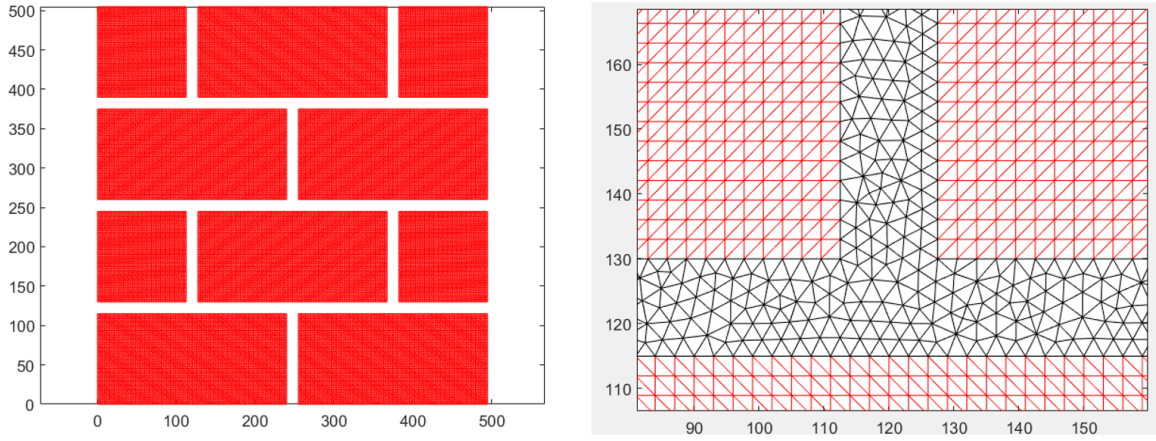

(a) The mesh (brick phase) (b) Zoom in of the mesh

Figure 9. Discretization of the tensile tests

In test T1, the load increment of $\Delta u = 0.0005$ mm for the 50 first step and $\Delta u = 0.0001$ mm for the next 250 steps. The crack pattern is shown in Fig. 9(a) for the end of simulation. Considering the material properties in Table 2, both elastic and fracture properties of mortar-interface is extremely smaller than that of units. Again, we can observe that cracks appear in the mortar-interface and create the zig-zag one, which was captured in a literature experiment, showed in Fig. 10(a) for the case SB-WM.

Table 2. Material properties for 3 tensile tests

Test	E_b (Mpa)	E_m/E_b	$\nu_b = \nu_m$	g_{cb} (N/mm)	g_{cm}/g_{cb}	Internal length l (mm)
T1	16700	0.5	0.15	0.06	0.1	10
T2	16700	1	0.15	0.06	0.1	10
T3	16700	1	0.15	0.06	0.5	10

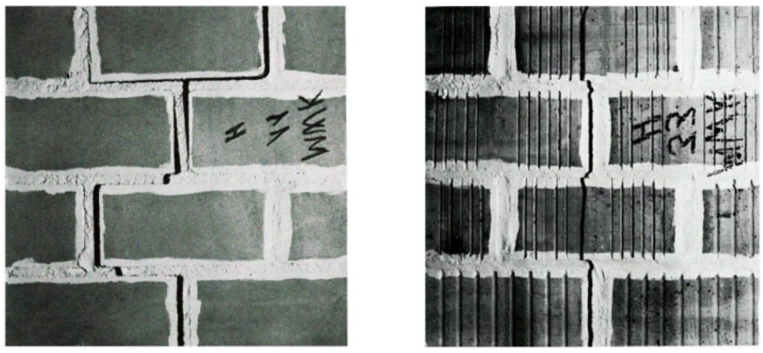

(a) Zig-zag crack (b) Straight crack

Figure 10. Crack pattern in tensile test: for SB-WM (a) and SM-WB (b) [16]

For test T2, the load increment is $u = 0.0005$ mm for the 100 first steps, $\Delta u = 0.0002$ mm for the next 100 steps, $\Delta u = 0.0001$ mm for the next 100 steps. The elastic properties in this case are harder

compared to the T1 test. The simulation captures a straight crack that traverses the weaker and the harder phases at the bottom of the sample. Based on the images, it is predicted to join with two other cracks on the top of the sample, forming a zig-zag line in the final simulation as shown in Fig. 11(b).

For test T3, the load increment of $\Delta u = 0.0005$ mm for the 50 first steps, $\Delta u = 0.0002$ mm for the next 50 steps, $\Delta u = 0.0001$ mm for the next 200 steps. The fracture toughness of the mortar-interface is the hardest among three cases. This results in a straight line as can be seen in Fig. 10(c). We can state that the straight crack in Fig. 5(b) (SM-WB) is captured in the case of test T3, when the fracture property of brick is not too larger than that of the mortar-interface.

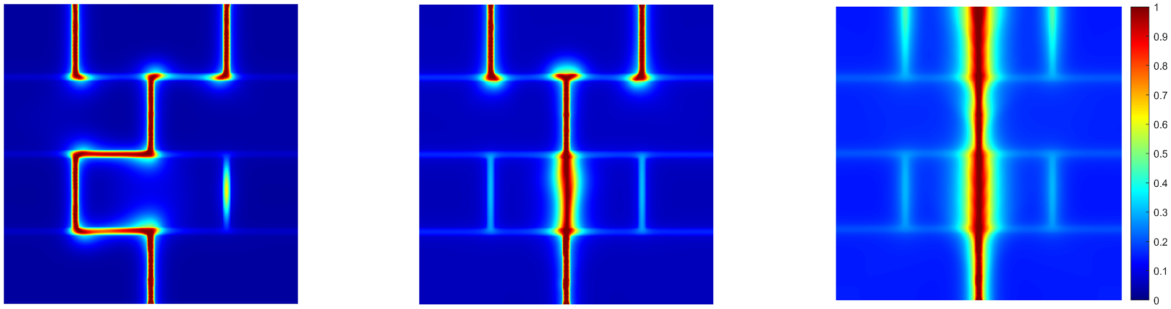

(a) T1 (b) T2 (c) T3

Figure 11. Crack patterns of tensile test in 3 cases of material properties:
(a) T1 test ($E_m = 0.5E_b, G_b = 10G_m$); (b) T2 test ($E_m = E_b, G_b = 10G_m$); (c) T3 test ($E_m = E_b, G_b = 2G_m$)

5. Conclusions

This study has presented a simplified micro approach for tracking cracks in masonry-like structures which are described as a two-phase material including the units and the mortar-interface. The interface between these two phases is accounted for by pseudo fracture parameters of the mortar-interface. Though this paper cannot cover all the strategies of materials, the results in numerical examples have demonstrated the advantages of the phase field method when studying complex fracture: (i) the phase field method can capture the onset of masonry-like structures without the presence of a notch or prior definition of cracks; (ii) cracks can branch and connect naturally; (iii) in both media, units and the mortar-interface, cracks can appear simultaneously without additional criteria. To the author's knowledge, limited works can capture cracks in both blocks and joints. This is the beauty of the model that encourages more studies. Future works may put efforts on (i) the determination of pseudo properties for the mortar-interface so that the force-displacement curve can be fitted with experiments, (ii) how the difference between characteristic length l between the two phases affect the crack pattern as it is interpreted a as material property, (iii) structures using the anisotropic material can studied using another phase field model, e.g. a stress-based phase field model.

References

[1] El-Maissi, A. M., Kassem, M. M., Tan, C. G., Fikri, R., Nazri, F. M. (2022). Damage index seismic assessment methodologies of URM buildings: A state-of-the-art review. *Engineering Journal*, 26(1): 39–53.

[2] Massart, T. J., Peerlings, R. H. J., Geers, M. G. D. (2007). Structural damage analysis of masonry walls using computational homogenization. *International Journal of Damage Mechanics*, 16(2):199–226.

[3] Lourenço, P. B., Rots, J. G., Blaauwendraad, J. (1998). Continuum model for masonry: parameter estimation and validation. *Journal of Structural Engineering*, 124(6):642–652.

[4] Nguyen, N., Tran, N. Q., Tran, B. A., Do, Q. H. (2021). On the respect to the Hashin-Shtrikman bounds of some analytical methods applying to porous media for estimating elastic moduli. *Journal of Science and Technology in Civil Engineering (STCE) - NUCE*, 15(2):14–25.

[5] Nhu, N. T. H., Binh, T. A., Hung, H. M. (2020). A three-dimensional model for rain-wind induced vibration of stay cables in cable-stayed bridges. *Journal of Science and Technology in Civil Engineering (STCE) - NUCE*, 14(1):15–27.

[6] Saloustros, S., Cervera, M., Pelà, L. (2017). Tracking multi-directional intersecting cracks in numerical modelling of masonry shear walls under cyclic loading. *Meccanica*, 53(7):1757–1776.

[7] Pelà, L., Cervera, M., Roca, P. (2013). An orthotropic damage model for the analysis of masonry structures. *Construction and Building Materials*, 41:957–967.

[8] Attard, M. M., Nappi, A., Tin-Loi, F. (2007). Modeling fracture in masonry. *Journal of Structural Engineering*, 133(10):1385–1392.

[9] Lourenço, P. B., Rots, J. G. (1997). Multisurface interface model for analysis of masonry structures. *Journal of Engineering Mechanics*, 123(7):660–668.

[10] Bažant, Z. P. (1991). Why continuum damage is nonlocal: Micromechanics arguments. *Journal of Engineering Mechanics*, 117(5):1070–1087.

[11] Nguyen, N., Yvonnet, J., Réthoré, J., Tran, A. B. (2018). Identification of fracture models based on phase field for crack propagation in heterogeneous lattices in a context of non-separated scales. *Computational Mechanics*, 63(5):1047–1068.

[12] Miehe, C., Hofacker, M., Welschinger, F. (2010). A phase field model for rate-independent crack propagation: Robust algorithmic implementation based on operator splits. *Computer Methods in Applied Mechanics and Engineering*, 199(45–48):2765–2778.

[13] Miehe, C., Welschinger, F., Hofacker, M. (2010). Thermodynamically consistent phase-field models of fracture: Variational principles and multi-field FE implementations. *International Journal for Numerical Methods in Engineering*, 83(10):1273–1311.

[14] Wambacq, J., Ulloa, J., Lombaert, G., François, S. (2022). A variationally coupled phase field and interface model for fracture in masonry. *Computers &Structures*, 264:106744.

[15] Francfort, G. A., Marigo, J.-J. (1998). Revisiting brittle fracture as an energy minimization problem. *Journal of the Mechanics and Physics of Solids*, 46(8):1319–1342.

[16] Bourdin, B., Francfort, G. A., Marigo, J.-J. (2008). The variational approach to fracture. *Journal of Elasticity*, 91(1–3):5–148.

[17] Wu, J.-Y., Nguyen, V. P. (2018). A length scale insensitive phase-field damage model for brittle fracture. *Journal of the Mechanics and Physics of Solids*, 119:20–42.

[18] Backes, H. P. (1985). Tensile strength of masonry. In *Proceedings of the 7th International Brick Masonry Conference*, Melbourne, Australia, 779–790.